BioEnergy Research
https://doi.org/10.1007/s12155-019-09993-6

Intraparticle Connectivity in Sugarcane Bagasse Unveiled by Pore Network Modeling

Daison Yancy-Caballero [1,2] · **Liu Y. Ling** [1] · **André Fujita** [2] · **João E. Ferreira** [2] · **Carlos Driemeier** [1]

Abstract

Sugarcane bagasse is a vast, inexpensive lignocellulosic feedstock that can be industrially converted into renewable materials, chemicals and biofuels. Bagasse, which results from the shredding and crushing of the sugarcane stalks, has a pore structure that is inherited from the native plant tissues and is partly disrupted due to the applied mechanical processes. The connectivity in the bagasse pore space can be critical for mass transport in industrial processes requiring liquid or solute extraction from the solid or impregnation of catalysts and reactants into the biomass. In this work, we pioneer the construction of pore network models (PNMs) to investigate intraparticle connectivity in lignocellulosic biomass. X-ray microtomograms of sugarcane bagasse are employed to extract the PNMs, which are then analyzed with support from hydraulic, diffusion, and graph theory-based methods. The analysis determines the characteristic sizes and anisotropies of the bagasse pore space. Moreover, it reveals that a relatively small number of pores are critical for the intraparticle connectivity. The critical pores can be in tissue cracks and xylem vessels as well as in ruptured parenchyma and fiber cells. The relative importance of each of these regions depends on the specifics of the bagasse particle.

Keywords Pore network modeling · Microtomography · Sugarcane · Bagasse · Biomass

Introduction

The world produces about 1.9 billion metric tons of sugarcane per year [1]. Once transported to the industry, sugarcane stalks are shredded and crushed to extract the juice, from which sugar and ethanol are produced [2, 3]. The fibrous by-product is the sugarcane bagasse. In dry-matter basis, bagasse corresponds to 12–14% of the sugarcane stalk tonnage, about 250 million metric tons per year if calculated from the global sugarcane production. Shredding and crushing aim at rupturing cells to release the cane juice. However, the rupture of the tissues is incomplete. The relatively fragile and juicy parenchyma cells are mostly ruptured, but the structural thick-walled fiber cells and epidermal tissues tend to preserve integrity. The partially disrupted tissues can hold water, which was shown to be located mostly inside such robust integer fiber cells of the fresh bagasse [4].

Bagasse is a heterogeneous particulate matter used mainly as boiler fuel in the sugarcane mills. However, there is surplus bagasse available at the processing site, making bagasse a vast, inexpensive, and underutilized renewable resource [3, 5]. Mass transport inside bagasse particles is important for processes such as sugar extraction [2], bagasse functionalization for usage in water treatment [6], and pretreatment for production of cellulosic biofuels [7, 8]. Moreover, the porosity of the biomass feedstock can be critical for production of porous bio-based materials [9, 10]. Intraparticle mass transport depends on the characteristics of the pore space. At the nanoscale, lignocellulosic biomass porosity is an attribute of plant cell walls and a function of the biomass hydration state and processing history [11, 12]. At the micrometer scale, porosity results from the cellular spaces delineated by the cell walls and, in sugarcane bagasse, the connectivity of the pore space is enhanced by the wall disruptions induced by the mechanical processing [13].

Modeling transport phenomena inside biomass has been advancing to consider realistic intraparticle morphologies [14]. However, when it comes to modeling the intricacies of

---

Electronic supplementary material The online version of this article (https://doi.org/10.1007/s12155-019-09993-6) contains supplementary material, which is available to authorized users.

✉ Carlos Driemeier
carlos.driemeier@ctbe.cnpem.br

[1] Brazilian Bioethanol Science and Technology Laboratory (CTBE), Brazilian Center for Research in Energy and Materials (CNPEM), P.O. Box 6192, Rua Giuseppe Máximo Scolfaro, no. 10.000, Campinas, SP 13083-970, Brazil

[2] Institute of Mathematics and Statistics (IME), University of São Paulo (USP), São Paulo, SP 05508-090, Brazil

the biomass pore space, methods based on finite elements and computational fluid dynamics using either Navier-Stokes or lattice Boltzmann approaches become computationally expensive. For complex pore geometries, pore network models (PNMs) have been developed and successfully applied in geology, petroleum, and environmental engineering to study soils and rocks [15–18]. PNMs approximate the porous medium by treating void spaces (larger pores) as spheres connected through throats (narrow constrictions) represented by cylinders [17, 19]. PNMs can reproduce the real topology of the pore space based on images acquired by serial sectioning [20], confocal laser scanning microscopy [21], and X-ray computed microtomography [22]. We highlight that microtomography is a non-invasive 3D imaging technique providing micrometric image resolution, which allows the delineation of the plant cell walls as well as localized ruptures of cells and tissues.

In this work, we consider the hypothesis that bagasse has critical limitations in intraparticle connectivity and that such limitations can explain process-relevant observations such as the need for comminution to achieve thorough chemical functionalization [6] or spatial heterogeneity in tissue deconstruction induced by mild chemical processes [8]. To advance the understanding of intraparticle connectivity, we perform this exploratory study where we extract pore network models (PNMs) from X-ray computed microtomographic images of sugarcane bagasse, which, to the best of our knowledge, is the first report of PNMs from lignocellulosic biomass. Noteworthy, because of the tissue ruptures, bagasse is an interesting model system to advance PNMs as a tool to investigate intraparticle connectivity in lignocellulosic biomass. Here, we show that bagasse PNMs inform on the characteristic sizes and anisotropy of the pore space. Moreover, with support from hydraulic, diffusion, and graph theory, we show that a relatively small number of pores are highly critical for transport through the bagasse PNMs.

Materials and Methods

Acquisition and Selection of X-Ray Microtomograms

This work uses X-ray microtomograms selected from the ones presented in a previous article [23]. Air-dried bagasse particles were selected from bulk particulates and then imaged at the

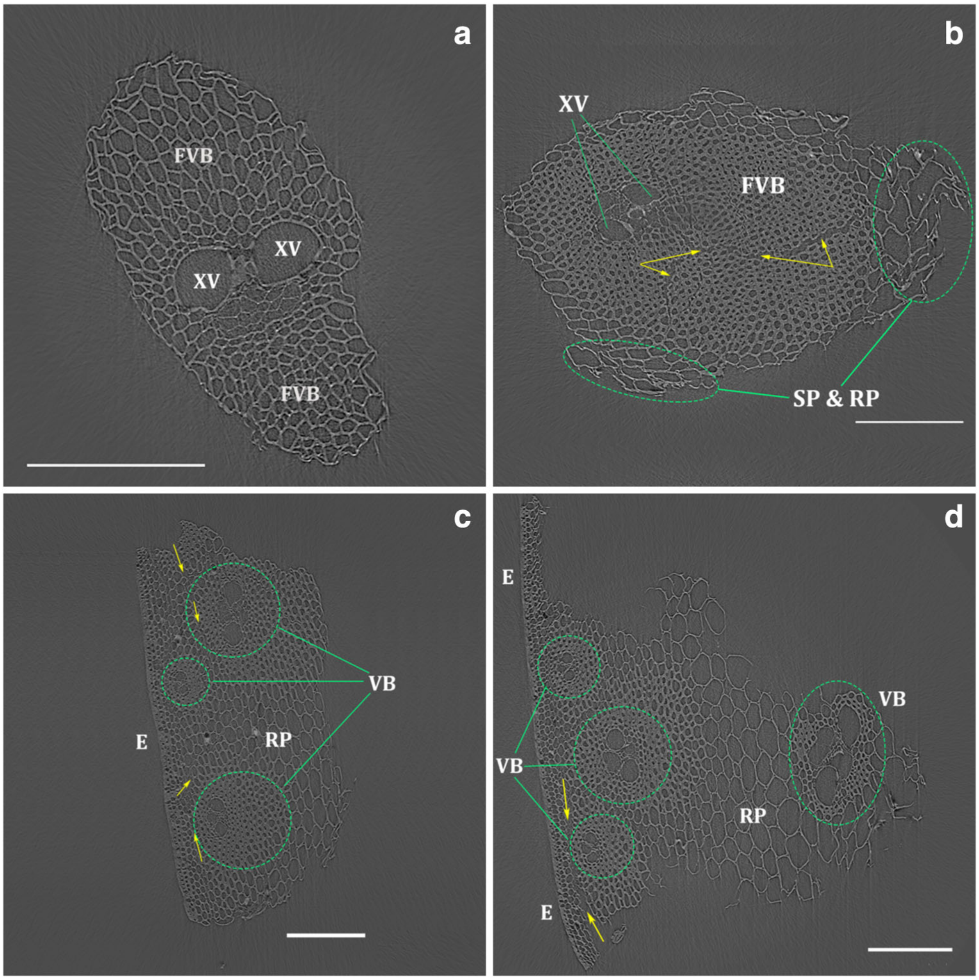

Fig. 1 Cross-section images of the analyzed sugarcane bagasse tomograms. **a**, **b** Pith particles showing one vascular bundle (VB). **c**, **d** Rind particles with respectively three and four VBs. Selected regions of round parenchyma (RP), smashed parenchyma (SP), fibers of vascular bundles (FVB), xylem vessel (XV), and epidermis (E) are indicated. Yellow arrows point to tissue cracks. Scale bars 200 µm

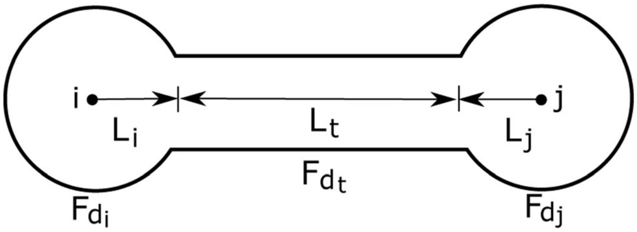

Fig. 2 Representation of the pore-throat-pore conduit

IMX beamline of the Brazilian Synchrotron Light Laboratory (LNLS) [24]. For each tomogram, 1001 projection images were captured by sample rotation from 0° to 180°. The 3D volume reconstruction was accomplished by using the PyHST software [25, 26]. The 3D images have voxel size of 0.82 μm and dimensions of 2048 × 2048 × 2048 voxels, generating a field of view of (1.68 mm)^3.

Guided by the broader image set from reference [23], we selected four tomographic images, namely T1–T4, for extraction of PNMs. Selection of T1–T4 images aimed at representing the most typical bagasse particles and their characteristic features. Characteristic cross sections are shown in Fig. 1. T1 (Fig. 1a) is a single vascular bundle without associated parenchyma cells. T2 (Fig. 1b) is also a single vascular bundle. Compared with T1, T2 has a denser sheath of sclerified fibers surrounding the xylem vessels and presents residual parenchyma cells associated to the periphery of the vascular bundle. T3 (Fig. 1c) and T4 (Fig. 1d) represent particles from the rind of sugarcane stalks, showing respectively three and four vascular bundles associated with parenchyma cells and epidermal tissue. Tissue cracks caused by mechanical disruption can be visualized in the T2–T4 cross-sections images (Fig. 1b–d).

Image Processing

Image processing employed the Thermo Scientific Avizo 9.4 Software. Pre-processing was performed with the Sobel edge-

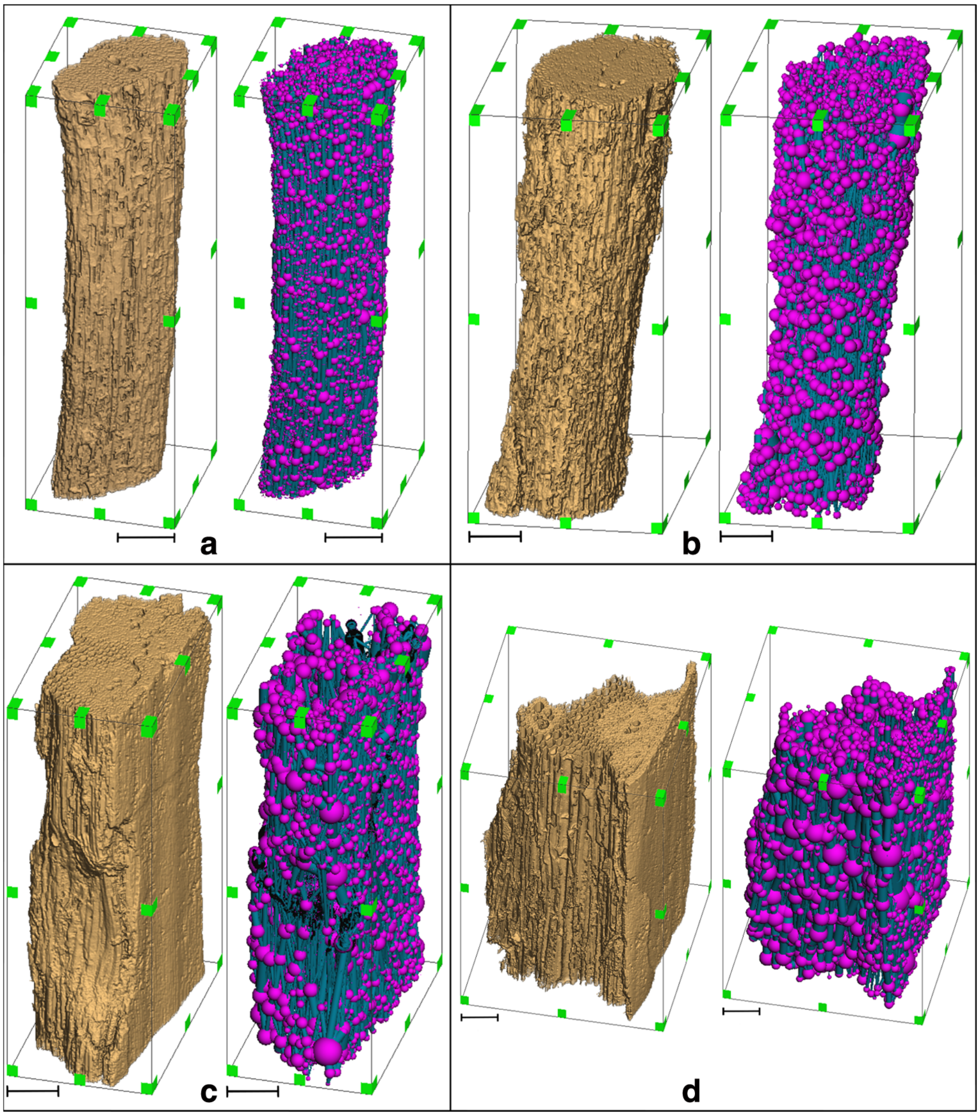

Fig. 3 Rendered views and extracted pore network models of the T1–T4 tomograms. Scalebars 200 μm

detection function for enhancement of cell wall edges and non-local means function for noise reduction. The region growing algorithm was employed to delineate the bagasse particle borders. Inside the borders, the particle volume was segmented as two phases: (i) the cell walls and (ii) the pore spaces. The cell walls were segmented using the watershed algorithm, with threshold value adjusted for each image. Finally, the segmented images were cleaned from islands inappropriately segmented as the wall phase. Such cleaning used the island removal function in combination with opening and closing morphological operators with a structuring element of 1 voxel. Visual inspection of the resulting segmented images (Fig. S1) shows that the basic cellular and tissue structures of the bagasse particles are preserved, but features of up to few micrometers can be artifacts introduced by image processing, reflecting the limitations in image contrast and resolution.

Extraction of Pore Network Models

The segmented 3D images were the basis for the extraction of PNMs. Generation of the PNMs employed modules available in the Avizo software. The whole procedure is summarized by the following steps: (1) removal of unconnected pores (because we will analyze connectivity), which was accomplished by the "Axis Connectivity" module with neighborhood and axis parameters set as 26 voxels and *z*-axis, respectively; (2) division of the pore space into a set of connected and labeled pores, which was accomplished by the "Separate Objects" module combined with the method parameter set as chamfer-conservative, which is well suited to separate spherical pores; (3) extraction of the PNM by using the "Generate Pore Network Model" module, which uses a variant of the maximal ball fitting algorithm [27].

The generated PNMs are all undirected weighted networks, meaning symmetrical cylindrical throats (network edges) connect pairs of spherical pores (network nodes) without directional paths. Radius R_p is attributed to each pore, while length L_t and radius R_t are attributed to each throat.

Weighting Throats by Hydraulic and Diffusive Conductivities

Mass transport theory for dissolved species or gas mixture in porous media considers terms of convection (due to bulk fluid flow by pressure gradients) and diffusion (due to the net molecular motion because of concentration gradients). These phenomena are generally modeled by the convection–diffusion equation [28]. However, this is a highly non-linear partial differential equation impractical to solve for porous media with the complexity of sugarcane bagasse. Hence, as an alternative approach, for each throat we calculate a weight F_g aiming at representing the conductance factor relevant for mass transport phenomena.

Table 1 Number of pores (network nodes) and throats (network edges) and the average degree of the connected PNMs

Tomogram	T1	T2	T3	T4
Number of pores	11,591	5272	3795	3120
Number of throats	23,224	20,945	20,522	16,059
Average degree	4.0	8.0	10.8	10.3

Concretely, we follow an approach that is widely applied to porous media represented by PNMs. Namely, the convection contribution is calculated by the Hagen–Poiseuille equation (valid for laminar flow) while the diffusion contribution is calculated by the Fick law [25, 29]. Although this work does not present any transport simulation, these concepts were used to define the conductance factors assigned as weights of the network throats. Let L_{ij} and R_{ij} be respectively the length and radius of the throat connecting pores i and j. Then, the hydraulic (F_h) and diffusive (F_d) conductance factors were calculated as

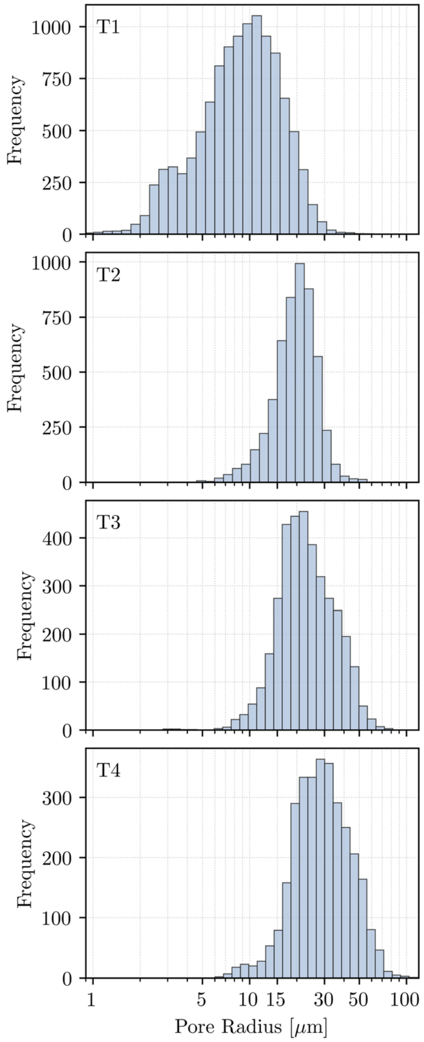

Fig. 4 Distributions of pore radii

$$F_h = \frac{\pi \cdot R_{ij}^4}{8 \cdot L_{ij}} \tag{1a}$$

$$F_d = \frac{\pi \cdot R_{ij}^2}{L_{ij}} \tag{1b}$$

respectively. The next step is to consider the conductance F_g of the pore-throat-pore conduit (Fig. 2), where the pore conductance (F_{di} and F_{dj}, for which we assume $L_p = R_p$) are combined with the throat conductance F_{dt} through the serial conductance formula,

$$\frac{1}{F_g} = \frac{1}{F_{d_i}} + \frac{1}{F_{d_t}} + \frac{1}{F_{d_j}} \tag{2}$$

In general, the conductance factors from the conduits are dominated by the contributions from the throats, which are longer and narrower than the pores.

Analysis of Network Centrality

Pore network centralities were analyzed with the NetworkX package [30], which is freely available as a Python package. Closeness and betweenness centralities

Fig. 5 Distributions of throat radii and lengths

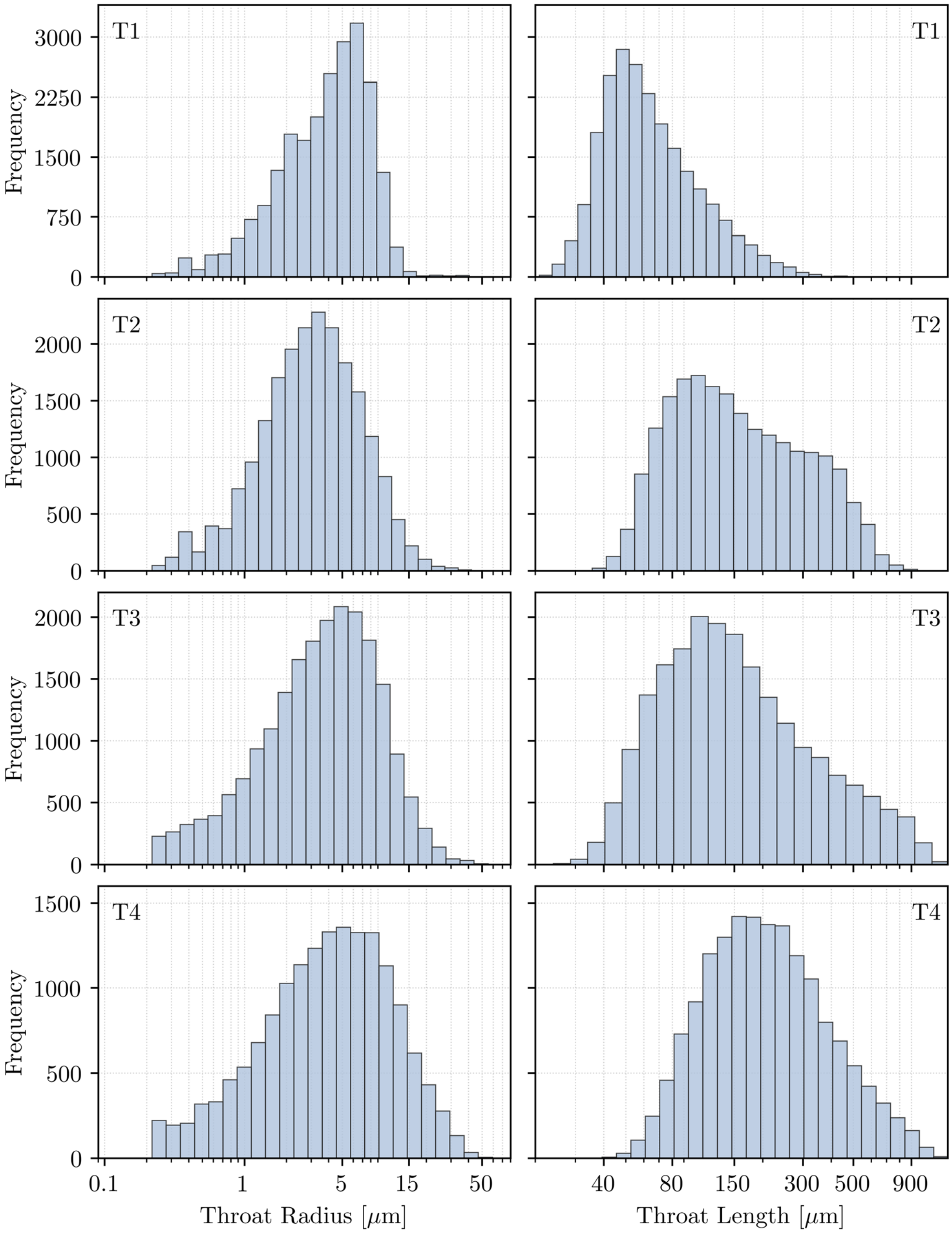

were calculated, in all cases with network edges (throats) weighted by either the hydraulic or the diffusive conductance factors calculated for the pore-throat-pore conduits (Eqs. 1, 2). Closeness centrality measures how close a node is from all other nodes, therefore accounting for the whole network. Betweenness centrality measures the fraction of all possible shortest (i.e., less resistant) paths between any pairs of nodes that pass through a specific node [31]. Therefore, betweenness centrality identifies nodes that concentrate a large share of the flow within the network.

Analysis of Network Clustering

Network cluster analysis employed the spectral clustering technique [32] coupled with the silhouette analysis [33], using the *R* statistical computing language and the igraph package (https://igraph.org). The spectral clustering technique allows determining how a network can be partitioned in clusters (communities) with high connectivity within each cluster and relatively low connectivity between distinct clusters. The number of clusters is an input of the spectral clustering technique, and the silhouette analysis was employed to determine suitable

Fig. 6 Scatter plot of throat lengths against throat angles. The left-hand side show data for all throats, while the right-hand side shows only throats with normalized diffusive conductance factor > 0.1

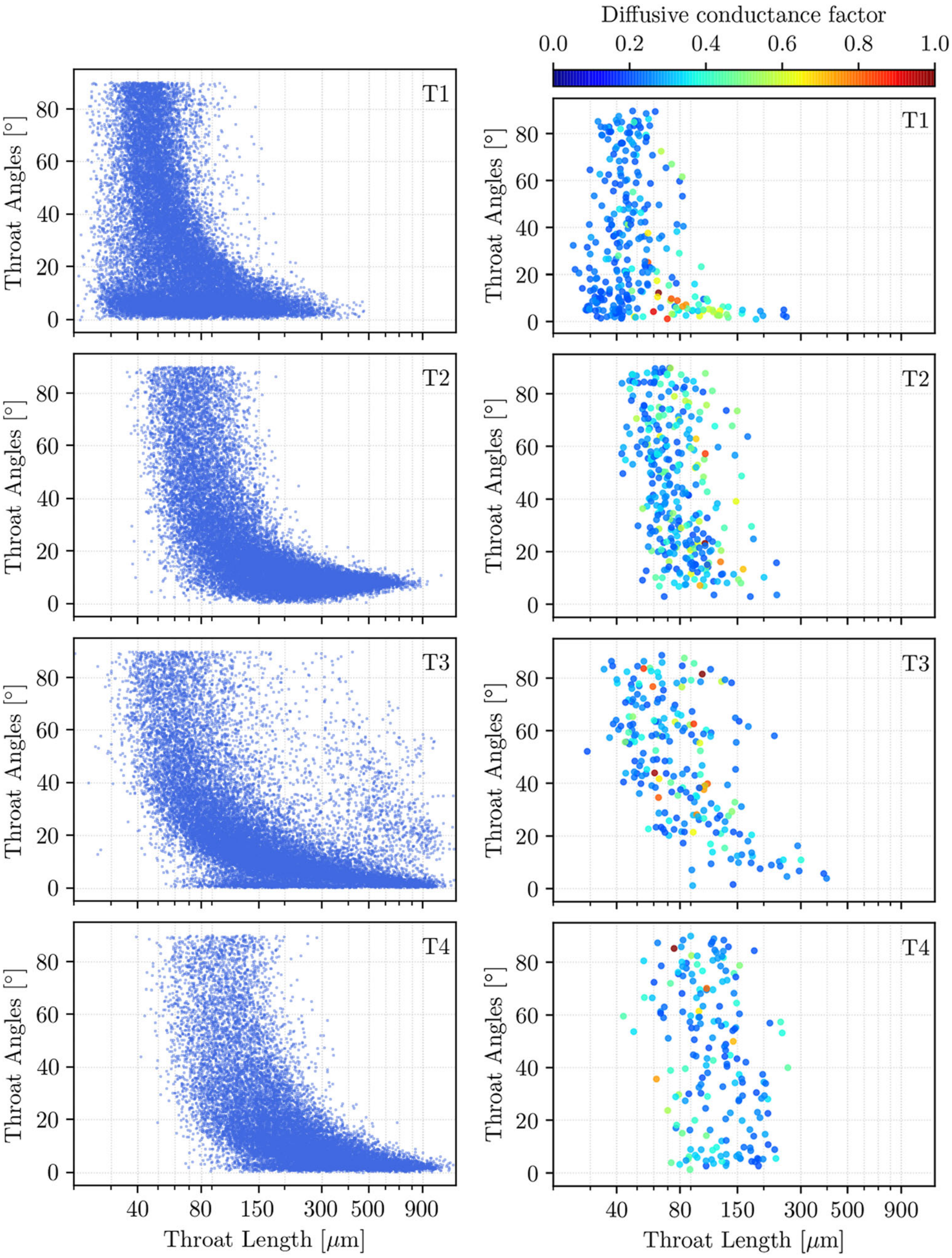

values for the number of clusters in each PNM. The spectral clustering technique along with the silhouette analysis was implemented in *R* by using the PAM function, which employs the *k*-medoids algorithm for clustering [34].

Classification of Pore Location

Pores of high betweenness centrality were classified according to the regions of sugarcane bagasse where they are located. This classification was done by visual inspection after marking the pore coordinates in the native gray-scale images. To each pore, one of the following location classes were assigned: (1) xylem vessels and surroundings; (2) tissue cracks and surroundings; (3) parenchyma cells; (4) fiber-parenchyma interface region; (5) fiber-epidermis interface region; and (6) fibers in vascular bundles. "Surroundings" and "interface regions" were defined to encompass a maximum thickness of two cells as observed in cross-section images (such as those of Fig. 1).

Results and Discussion

Visualization of the Connected Pore Networks

Figure 3 shows rendered views of the T1–T4 microtomograms and the PNMs generated from them. The PNM visualizations show pores as pink spheres and throats as blue cylinders, with their sizes scaled in proportion to R_p (pores), L_t and R_t (throats). From visual inspection of Fig. 3, we observe that PNMs contain large number of connected pores, which form a representation that is much simpler than the original particle images. Moreover, PNMs reproduce the volume of the bagasse particles, demonstrating that the connected PNMs are extended through most of the particles volumes despite neglecting the large number of small isolated pores (Figs. S2–3). We can also notice that most throats are aligned close to the vertical axis of the bagasse particles, reflecting the preferential orientation of the fibrous plant tissues.

Statistics of Pores and Throats

The number of pores and throats in each connected PNM is presented in Table 1 together with the network average degrees (twice the number of throats divided by the number of pores). The numbers for T1 are markedly different from those for T2–T4. T1 has more than double the number of pores (11,591 in T1 compared with 5272-3120 in T2–T4) and lower average degree (4.0 in T1 compared with 8.0–10.8 in T2–T4).

T1 also differs from T2–T4 in the distribution of pore radii (Fig. 4). The more numerous pores of T1 seems to come mainly from a lower range of pore radius, circa 1–10 µm (Fig. 4). Except for this marked difference in T1, the other distributions of pore radii are quite similar to one another. In another relatively minor difference, more numerous pores are observed in the high-end of pore size (radius from 50 to 100 µm) in the rind particles (T3 and T4). These larger pores are presumably associated with the parenchyma cells that have such size range and are present in significant numbers in the rind particles T3–T4 (see Fig. 1).

Interesting similarities and differences are also observed in the distributions of throat dimensions (Fig. 5). Distributions of throat radii are quite similar for T1–T4. Noteworthy, significant number of throats is observed with radius close to or less than 1 µm. Due to limitations in image resolution, information associated with this size range is inherently uncertain. As for throat lengths, it is noteworthy that maximum lengths around 900 µm corresponds to about half of the image field of view in

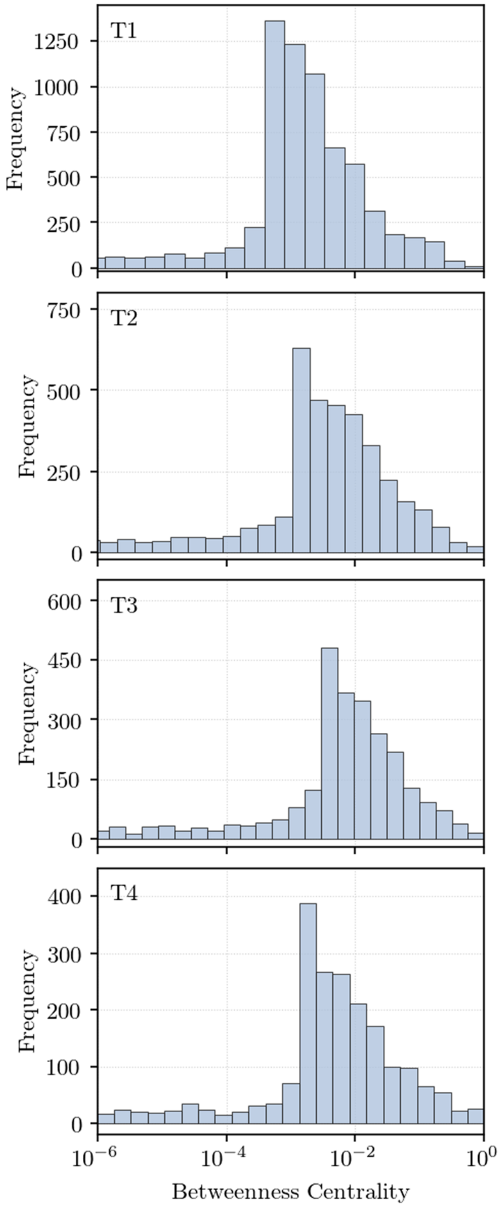

Fig. 7 Distributions of betweenness centrality using diffusive conductance factors as throat weights

each spatial direction (1.68 mm). Moreover, the distributions of throat lengths are markedly different for T1, which present shorter throats (circa 20–80 μm) with higher frequencies than found in T2–T4. Once again, this difference of T1 is consistent with the higher number of pores (Table 1). If more pores need to be connected in a similar 3D volume, the connections will tend to be shorter, as observed.

Another relevant feature is the throat angle with respect to the image *z*-axis, which is aligned close to the bagasse fiber axis. For all the PNMs (T1–T4), the angular distributions are peaked at low (0–10°) angles (Fig. S4), demonstrating the preferential alignment of the throats with the bagasse fiber axis. However, the relations between throat length, angle, and conductivity have nuances that will be important for transport inside the bagasse particle. The left-hand side of Fig. 6 shows the scatter plots of angle against length for all the throats of the T1–T4 PNMs. Most of the longer throats ($L_t >$ 300 μm) are aligned to fiber axis (angle < 20°). When we consider the conductance factors (Eqs. 1–2), which will determine the actual relevance of a given throat, those long and aligned throats loose relevance. For hydraulic (Fig. S5) and diffusive (Fig. 6) conductance factors, the right-hand side of the figures show the same scatter plot, but data points are colored according to normalized (from 0 to 1) conductance factor and only those throats with factors > 0.2 are kept in the plot. With this conductance cutoff, the picture changes: throats from all angles (0–90°) are well represented and the range of length is much narrower, from about 40–200 μm.

Network Centrality

So far, pore and throat statistics considered the full set of individual pores and throats (Figs. 4–6) but did not consider metrics reflecting collective behaviors of the networks. Closeness and betweenness centralities of each pore are calculated considering the whole PNM, and therefore, these metrics inform on such collective network properties. Moreover, the calculations of centrality are all weighted by the conductance factors (Eqs. 1, 2), and therefore, the network edges are counted with consideration of their conductance, which minimizes the contribution from the narrow (R_t ~< 1 μm) and uncertain throats (Fig. 5). In the distributions of closeness centrality (Fig. S6), virtually all the pores from the T1–T4 PNMs have (normalized) closeness centrality between 0.2 and 1.0. That is, virtually all pores are quite accessible from

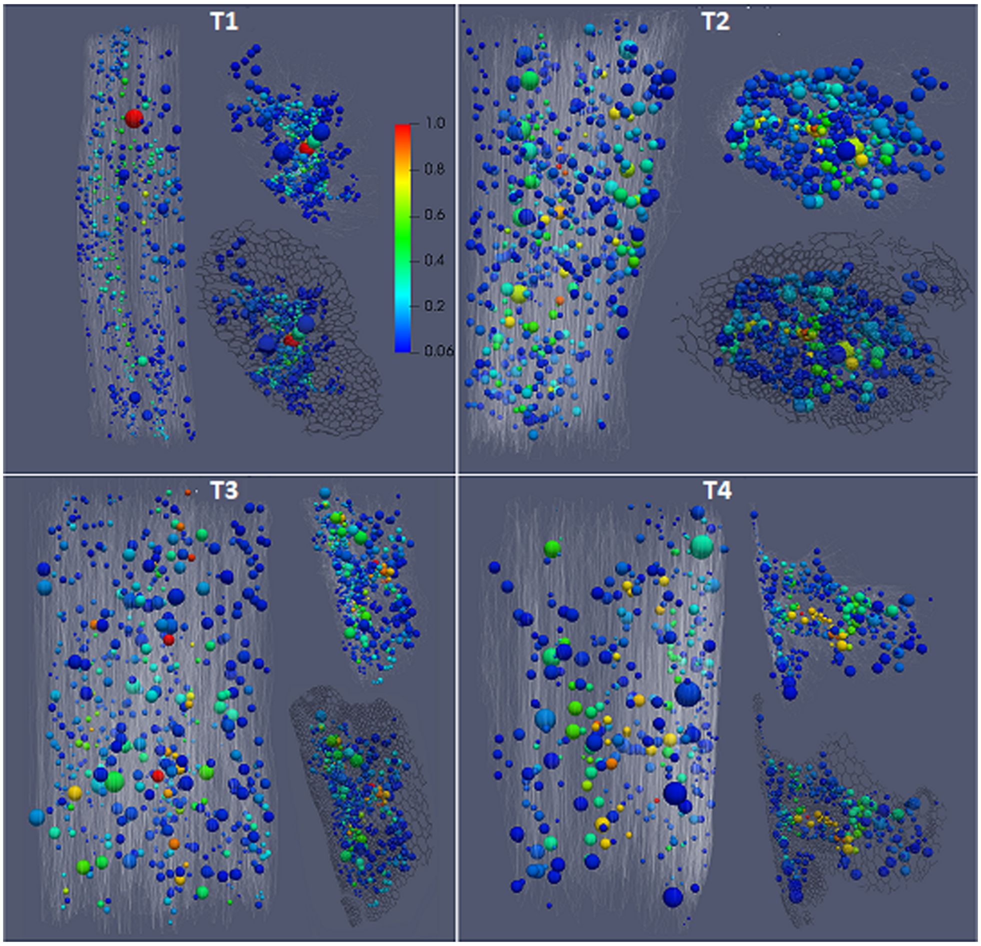

Fig. 8 Longitudinal and cross-sectional projections of the pores having normalized betweenness centrality between 0.06 and 1. Spheres are scaled according to pore size and color represents betweenness centrality. Cross-section projections are overlapped with cross-section images to serve as visual references to approximate the pore location in the native images

Table 2 Location of top 10 and top 100 pores ranked by betweenness centrality in the T1–T4 networks

Pore location	Top 10				Top 100			
	T1	T2	T3	T4	T1	T2	T3	T4
Xylem vessel and surroundings	7	0	1	5	53	23	13	18
Tissue crack and surroundings	0	9	1	0	0	33	7	5
Parenchyma cells	0	0	0	1	0	0	21	15
Fiber-parenchyma interface region	0	0	6	4	0	20	41	47
Fiber-epidermis interface region	0	0	1	0	0	0	11	8
Fibers in vascular bundles	3	1	1	0	47	24	7	7
Total	10	10	10	10	100	100	100	100

the rest of the network, with variations of closeness centrality kept within one order of magnitude.

On the other hand, the distributions of betweenness centrality show different shapes of the histograms (Fig. 7), and a relatively small number of pores have betweenness centrality much higher than rest of the network. It is key to remark the logarithm scale of the betweenness centralities presented in Fig. 7. As stated in the method section, betweenness centrality is a metric that seeks those pores more important for the transport through the network, not because of the number of connections (coordination number), but because the pore belongs to many paths of lowest resistance connecting different regions of the network. In each PNM, a relatively small number of pores have betweenness centrality between 10^{-1} and 10^{0}. As we move to lower centralities, the frequency increases until it peaks at centralities around 10^{-3}, and then it drops to much lower frequencies. This result shows that a relatively small number of pores (those with the highest centralities) mediate a large share of the connectivity within the bagasse particles.

Recognizing the importance of the pores of high betweenness centrality, we evaluate where they are in the bagasse particles. Figure 8 shows longitudinal and transversal projection views of the T1–T4 PNMs, showing the pores with normalized betweenness centrality in the 0.06–1 range. One first notes that the presented pores are quite well distributed along the length of the particles, while in cross-sections the pores tend to be located closer to the particle center, with peripheries being less populated. Since the pores were selected based on betweenness centrality, one could expect that pores closer to the geometric center of the particle would be more numerous. Therefore, it is interesting that this effect is notable at cross-sections but not across particle lengths.

The top 10 and top 100 pores ranked by betweenness centrality were localized with high precision by marking their coordinates in the native gray-scale images. Classification of pore location is presented in Table 2. Let us first compare the single vascular bundles (T1–T2) from sugarcane pith. T1 has no crack, no parenchyma and no epidermis (Fig. 1a). Therefore, its connectivity is fully represented by the regions of xylem vessels and fibers, as observed in Table 2. Interestingly, fibers of the T1 vascular bundle shows significant connectivity, demonstrating localized fiber ruptures that create interfiber connections. On the other hand, T2 has a set of cracks through the fiber sheath (Fig. 1b) and these cracks dominate the top 10 pores. This demonstrates how important cracks can be to permeate the fiber sheaths. Looking to the top 100 pores, xylem vessels and fibers are also well ranked in T2. Interestingly, the parenchyma-fiber interface also appears in the top 100 rank, although there is little parenchyma associated to the T2 vascular bundle (Fig. 1b).

For the rind particles (T3–T4), all the regions are represented in the top 100 rank (Table 2). The surprising contribution comes from the fiber-parenchyma interface regions, which represents about half of the top 10 pores and little less than half of the top 100 pores (Table 2). Interestingly, the region of fibers in vascular bundles (more distant from parenchyma) are much less represented in the T3–T4 ranking. The sheath of thick-walled fibers in vascular bundles tends to be the most integer and least connected region of bagasse particles. If so, there might be localized critical pathways that can penetrate the fiber sheaths, either through extended tissue cracks (like in T2) or through a set of adjacent ruptured fibers. We speculate

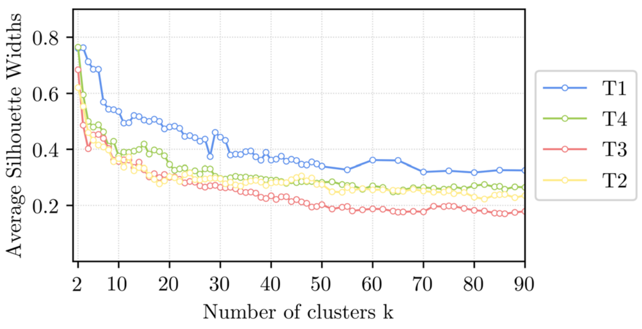

Fig. 9 Average silhouette widths as function of the number of clusters for the T1–T4 tomograms

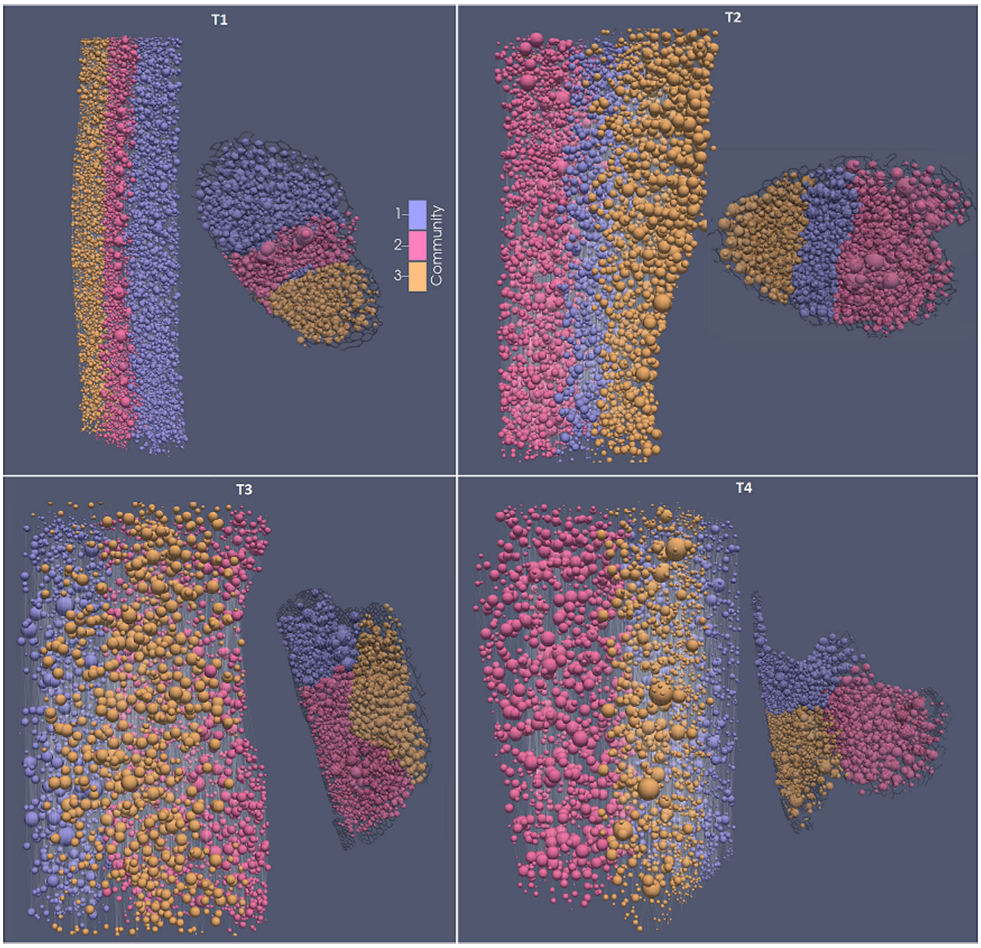

Fig. 10 Spectral clustering algorithm was employed to partition the pores of each network in three clusters. For all the T1–T4 networks, the clusters extend through the entire particle length, whereas the particle cross-sections are partitioned in distinct clusters

the critical pores in the fiber-parenchyma interface region are localized gateways into the vascular bundle fiber sheath.

Network Clustering

Figure 9 shows the average silhouette widths with the number of cluster k varying from 2 to 90 for each one of the PNMs. For T1–T4, the average silhouette widths decrease as the number of clusters increase. The optimal choice for the number of clusters is given by the largest silhouette width [33], i.e., $k = 2$ or 3 being acceptable choices for all T1, T2, T3, and T4.

We chose to partition each PNM into three clusters. The spatial distributions of the clusters can be visualized in Fig. 10. All the clusters are distributed across the full particle lengths, while the partitioning takes place in the particles cross-sections. This result shows that the anisotropy of the fibrous tissues creates stronger connectivity along the fiber axis and, therefore, in all cases, partitioning occurs across the less connected transversal plane.

Conclusion

This work performed an exploratory investigation that serves as foundation for the application of PNMs to investigate mass transport inside lignocellulosic biomass. As a first result, we recognize that the quality and resolution of the experimental images set the practical limits for the smallest pores and narrowest throats that can be reliably evaluated in biomass PNMs. Second, the descriptive statistics of pores and throats (number, radius, length, and angle) inform on the characteristic size and anisotropy of the pore space, being an alternative to conventional approaches for morphometry based on image analysis. Third, the remarkable novelty brought by PNMs is the possibility of understanding collective characteristics of the pore space such as those informed by network clustering and betweenness centrality. For the bagasse particles investigated in this work, clustering showed continuity across particle length but partitioning at cross-sections, demonstrating the tissue anisotropy with higher connectivity along the fiber axis. In addition, analysis of betweenness centrality indicated that large share of the network flow is concentrated in a small number of pores, which are thus pivotal for intraparticle mass transport. Vessels and cracks as well as parenchyma and fibers occasionally appeared as critical pores, with the relative importance of these regions depending on the specifics of each bagasse particle.

Acknowledgments LNLS is acknowledged for the microtomography beamtime (proposal IMX 20160061). Information Technology Superintendence of the University of São Paulo is acknowledged for the high-performance computing resources.

Funding Information FAPESP is acknowledged for their financial support (grants 2015/01587-0 and 2017/01330-5).

References

1. FAOSTAT database. http://www.fao.org/faostat/en/
2. Rein P (2007) Cane sugar engineering. Verlag Dr. Albert Bartens KG, Berlin
3. Cortez LAB (2010) Sugarcane bioethanol: R&D for productivity and sustainability. Blucher, São Paulo
4. Driemeier CE, Ling LY, Yancy-Caballero D, Mantelatto PE, Dias CSB, Archilha NL (2018) Location of water in fresh sugarcane bagasse observed by synchrotron X-ray microtomography. PLoS One 13:e0208219. https://doi.org/10.1371/journal.pone.0208219
5. Soccol CR, Vandenberghe LPDS, Medeiros ABP et al (2010) Bioethanol from lignocelluloses: status and perspectives in Brazil. Bioresour Technol 101:4820–4825. https://doi.org/10.1016/j.biortech.2009.11.067
6. Karnitz O, Gurgel LVA, de Melo JCP et al (2007) Adsorption of heavy metal ion from aqueous single metal solution by chemically modified sugarcane bagasse. Bioresour Technol 98:1291–1297. https://doi.org/10.1016/j.biortech.2006.05.013
7. Wyman CE (2013) Aqueous pretreatment of plant biomass for biological and chemical conversion to fuels and chemicals. Wiley, Chichester
8. Lima CS, Rabelo SC, Ciesielski PN, Roberto IC, Rocha GJM, Driemeier C (2018) Multiscale alterations in sugar cane bagasse and straw submitted to alkaline deacetylation. ACS Sustain Chem Eng 6:3796–3804. https://doi.org/10.1021/acssuschemeng.7b04158
9. Xu A-R, Chen L, Guo X, Xiao Z, Liu R (2018) Biodegradable lignocellulosic porous materials: fabrication, characterization and its application in water processing. Int J Biol Macromol 115:846–852. https://doi.org/10.1016/j.ijbiomac.2018.04.133
10. Xu A, Chen L, Wang J (2018) Functionalized imidazalium carboxylates for enhancing practical applicability in cellulose processing. Macromolecules 51:4158–4166. https://doi.org/10.1021/acs.macromol.8b00724
11. Maziero P, Jong J, Mendes FM, Gonçalves AR, Eder M, Driemeier C (2013) Tissue-specific cell wall hydration in sugarcane stalks. J Agric Food Chem 61:5841–5847. https://doi.org/10.1021/jf401243c
12. Hinkle JD, Ciesielski PN, Gruchalla K, Munch KR, Donohoe BS (2015) Biomass accessibility analysis using electron tomography. Biotechnol Biofuels 8:212. https://doi.org/10.1186/s13068-015-0395-8
13. Isaac A, Sket F, Driemeier C, Rocha GJM (2013) 3D imaging of sugarcane bagasse using X-ray microtomography. Ind Crop Prod 49:790–793. https://doi.org/10.1016/j.indcrop.2013.07.005
14. Ciesielski PN, Crowley MF, Nimlos MR, Sanders AW, Wiggins GM, Robichaud D, Donohoe BS, Foust TD (2015) Biomass particle models with realistic morphology and resolved microstructure for simulations of intraparticle transport phenomena. Energy Fuel 29:242–254. https://doi.org/10.1021/ef502204v
15. Blunt MJ (2001) Flow in porous media—pore-network models and multiphase flow. Curr Opin Colloid Interface Sci 6:197–207. https://doi.org/10.1016/S1359-0294(01)00084-X
16. Bultreys T, Van Hoorebeke L, Cnudde V (2015) Multi-scale, micro-computed tomography-based pore network models to simulate drainage in heterogeneous rocks. Adv Water Resour 78:36–49. https://doi.org/10.1016/j.advwatres.2015.02.003
17. Xiong Q, Baychev TG, Jivkov AP (2016) Review of pore network modelling of porous media: experimental characterizations, network constructions and applications to reactive transport. J Contam Hydrol 192:101–117. https://doi.org/10.1016/j.jconhyd.2016.07.002
18. Xie C, Raeini AQ, Wang Y, Blunt MJ, Wang M (2017) An improved pore-network model including viscous coupling effects using direct simulation by the lattice Boltzmann method. Adv Water Resour 100:26–34. https://doi.org/10.1016/j.advwatres.2016.11.017
19. Blunt MJ, Jackson MD, Piri M, Valvatne PH (2002) Detailed physics, predictive capabilities and macroscopic consequences for pore-network models of multiphase flow. Adv Water Resour 25:1069–1089. https://doi.org/10.1016/S0309-1708(02)00049-0
20. Vogel H-J, Roth K (2001) Quantitative morphology and network representation of soil pore structure. Adv Water Resour 24:233–242. https://doi.org/10.1016/S0309-1708(00)00055-5
21. Tomutsa L, Silin DB, Radmilovic V (2007) Analysis of chalk Petrophysical properties by means of submicron-scale pore imaging and modeling. SPE Reserv Eval Eng 10:285–293. https://doi.org/10.2118/99558-PA
22. Spanne P, Thovert JF, Jacquin CJ, Lindquist WB, Jones KW, Adler PM (1994) Synchrotron computed microtomography of porous media: topology and transports. Phys Rev Lett 73:2001–2004. https://doi.org/10.1103/PhysRevLett.73.2001
23. Yancy-Caballero D, Ling LY, Archilha NL, Ferreira JE, Driemeier C (2017) Mineral particles in sugar cane bagasse: localization and morphometry using microtomography analysis. Energy Fuel 31:12288–12296. https://doi.org/10.1021/acs.energyfuels.7b02247
24. Schubert G, Vasconcelos GJQ, Dias CS, Archilha NL, Miqueles EX, O'Dowd FP (2017) IMX Beamline: X-ray Imaging, Version 0.1.; CNPEM – Centro Nacional de Pesquisa em Energia e Materiais / LNLS - Laboratório Nacional de Luz Síncrotron: Campinas, Brazil
25. Chilingaryan S, Mirone A, Hammersley A, Ferrero C, Helfen L, Kopmann A, dos Santos Rolo T, Vagovic P (2011) A GPU-based architecture for real-time data assessment at synchrotron experiments. IEEE Trans Nucl Sci 58:1447–1455. https://doi.org/10.1109/TNS.2011.2141686
26. Mirone A, Brun E, Gouillart E, Tafforeau P, Kieffer J (2014) The PyHST2 hybrid distributed code for high speed tomographic reconstruction with iterative reconstruction and a priori knowledge capabilities. Nucl Instruments Methods Phys Res Sect B Beam Interact with Mater Atoms 324:41–48. https://doi.org/10.1016/j.nimb.2013.09.030
27. Dong H, Blunt MJ (2009) Pore-network extraction from micro-computerized-tomography images. Phys Rev E 80:36307. https://doi.org/10.1103/PhysRevE.80.036307
28. Civan F (2011) Porous media transport phenomena. Wiley, Hoboken

29. Song W, Yao J, Ma J, Couples G, Li Y (2017) Assessing relative contributions of transport mechanisms and real gas properties to gas flow in nanoscale organic pores in shales by pore network modelling. Int J Heat Mass Transf 113:524–537. https://doi.org/10.1016/j.ijheatmasstransfer.2017.05.109
30. Hagberg AA, Schult DA, Swart PJ (2008) Exploring network structure, dynamics, and function using network. In: Proceedings of the 7th Python in science conference. Pasadena, pp 11–15
31. Delmas E, Besson M, Brice M-H, Burkle LA, Dalla Riva GV, Fortin MJ, Gravel D, Guimarães PR Jr, Hembry DH, Newman EA, Olesen JM, Pires MM, Yeakel JD, Poisot T (2019) Analysing ecological networks of species interactions. Biol Rev 94:16–36. https://doi.org/10.1111/brv.12433
32. von Luxburg U (2007) A tutorial on spectral clustering. Stat Comput 17:395–416. https://doi.org/10.1007/s11222-007-9033-z
33. Rousseeuw PJ (1987) Silhouettes: a graphical aid to the interpretation and validation of cluster analysis. J Comput Appl Math 20:53–65. https://doi.org/10.1016/0377-0427(87)90125-7
34. Kaufman L, Rousseeuw P (1987) Clustering by means of medoids. In: Dodge Y (ed) Statistical data analysis based on the L1 norm and related methods. North-Holland, Amsterdam